48th AIAA Aerospace Sciences Meeting Including the New Horizons Forum and Aerospace Exposition
4 - 7 January 2010, Orlando, Florida

AIAA 2010-726

A Numerical Study of Vortex-Dominated Flow around an Oscillating Airfoil with High-Order Spectral Difference Method

M. L. Yu[1], H. Hu[2] and Z. J. Wang[3]
Department of Aerospace Engineering, Iowa State University, Ames, IA 50011

A high-order spectral difference flow solver for compressible three-dimensional Navier-Stokes (N-S) equations has been utilized to numerically simulate the unsteady flow over the NACA 0012 airfoil undergoing a sinusoidal pitching motion at the Reynolds (Re) number of 12600. The effects of the reduced frequency and Strouhal number on the wake vortex structure and force coefficient have been studied. The force coefficients under different aerodynamic conditions agree well with experimental results. It was found that the wake vortex structure and thrust coefficient can be attributable to the combined effects caused by the reduced frequency and the Strouhal number. A relatively larger Strouhal number can easily induce moderate leading edge separation, which can generate larger thrust; A relatively smaller reduced frequency corresponds to a lower shear strain rate in the wake, which can also generate larger thrust. A deflected wake appears at large Strouhal numbers and the behavior of the deflected wake is greatly influenced by the initial conditions. A simple model was developed to explain the generation of the deflected wake, and it appears that the dipole acceleration could serve as a reason for the larger thrust generation at a larger Strouhal number. In addition, it was found that the compressibility of the fluid has an influence on the force coefficient. Based on this observation, all numerical simulations are performed with an inlet Mach number of 0.1, which has been verified to be reasonable for the present study. Moreover, in order to minimize the errors from dynamic grids, the effect of the Geometric Conservation Law (GCL) has been investigated in the ongoing research.

Nomenclature

A	=	Peak to peak amplitude of the airfoil's trailing edge
C	=	Chord length (=1)
T	=	Thrust force
S	=	Wing platform area
U_∞	=	Incoming flow velocity
ρ	=	Air density
ω	=	Angular velocity of pitching motion
C_T	=	Thrust coefficient, $T/(0.5\rho U_\infty^2 S)$
Re	=	Reynolds number, $\rho U_\infty C/\mu$
Ma	=	Mach number, $U_\infty/\sqrt{\gamma RT}$
f	=	Natural oscillating frequency
k	=	Reduced frequency, $\omega C/(2U_\infty)$
St	=	Strouhal number, fA/U_∞

I. Introduction

It was observed that in natural flights within the Reynolds number range of 10^3 to10^6, a thrust can be generated from flapping wing motions including both pitching and plunging motions. In order to study the inherent

[1] Graduate Research Assistant, Aerospace Engineering, 0247 Howe Hall, mlyu@iastate.edu, AIAA student member.
[2] Associate Professor, Aerospace Engineering, 2251 Howe Hall, huhui@iastate.edu, AIAA senior member.
[3] Professor, Aerospace Engineering, 2249 Howe Hall, zjw@iastate.edu, Associate Fellow of AIAA.

mechanisms of such kind of bio-inspired unsteady flow and in turn, to apply them in the design of Unmanned Aerial Vehicles (UAVs) and Micro-Air-Vehicles (MAVs), myriads of experiments and numerical simulations have been carried out recently[1-13]. Reports from the literature[14-17] have shown that these unsteady flows are dominated by moving vortices, which play a critical role in the flow characteristics. As 1st and 2nd order flow solvers may dissipate the unsteady vortices, we use a high-order spectral difference method in tackling the unsteady vortex-dominated flows.

Generally speaking, thrust generation from flapping motion is due to the reverse von Karman vortex street. Recently, Bohl and Koochesfahani[1] have experimentally studied the flow features with various reduced frequencies. Meanwhile, extensive numerical simulations have been performed by Young and Lai[2,3], who have focused on studying the relationships between flow features and the aerodynamic parameters. They have reported that in the numerical simulations with the compressible flow solver, the Mach number could affect the force coefficient significantly. Ellenrieder et al.[4] have emphasized the Strouhal number dependency of the wake vortex structure behind a translating airfoil. Godoy-Diana et al.[5] have experimentally studied the aerodynamic parameter dependency of the transition process from the drag-generation wake to the thrust-generation one. Kang et al.[6-7] have investigated the Reynolds number's effects on the flow structures. Hu et al.[8] have done experiments to study the effects of flexible wings on flapping flight. They have found that the thrust generated by flapping wings exponentially increases with the Strouhal number. However, it is still an open question to resolve the dependency of such bio-inspired flow on the aforementioned aerodynamic parameters.

Meanwhile, nonsymmetrical vortex shedding is another phenomenon which needs to be further studied. It was suggested by Jones et al.[9] that a deflected wake occurs generally with relative higher Strouhal number. (in their case, they use kh as the dominant parameter, which is equal to Strouhal number). But in their study, only a panel code is used to predict this phenomenon. Platzer et al.[10] suggested that under such flow conditions a viscous flow solver is necessary to provide a complete picture of the occurrence of the deflected wake structure. Lewin and Haj-Hariri[11] have used an incompressible viscous flow solver to study the aerodynamic parameter dependency of thrust generation for a heaving airfoil. Nonperiodic solutions are found in their research. Ellenrieder and Pothos[12] have experimentally verified the onset of the deflected wake and the corresponding flow features. However, the mechanism of the formation of the deflected wake remains an open problem. Furthermore, the deflected wake is usually accompanied with larger thrust, which means that fully understanding the characteristics of this phenomenon might be of great benefit for the design and control of UAVs and MAVs.

In order to model the phenomena relating to the symmetric breaking of the reversed von Karman vortex street, Godoy-Dinan et al.[13] have performed PIV experiments. Based on their results, they developed a 'dipole' model to explain the occurrence of the deflected wake. To some extent, this model can explain some phenomena relating to the deflected wake.

As mentioned above, in order to capture the detailed features of the vortex dominated flow more precisely, an efficient high-order method is necessary. The spectral difference (SD) method[17, 21, 22] used in the present study has been developed and demonstrated for vortex-dominated flows[18-20]. The basic approach to achieve high-order accuracy in the SD method is to use a high degree polynomial to approximate the exact solution in a local element (a standard cell). However, not like the discontinuous Galerkin (DG) method[17] and spectral volume (SV) method[17], the SD method is in the differential form, which is efficient and simple to implement. Since a curvilinear transformation from the physical domain to the standard element is needed in the SD method, the Geometric Conservation Law (GCL)[26] should be strictly satisfied in order to eliminate the grid motion induced errors. The GCL has been emphasized by many researchers[16, 23, 25]. For example, Visbal[27] has successfully utilized a high-order method (a compact finite-difference approach) to simulate the flow field around a SD7003 airfoil.

Based on the above discussions, the present paper endeavors to further study the coherent relationships between flapping motions and the aerodynamic parameters with the high-order SD method. Furthermore, this paper pays much attention to study how the occurrence of the deflected wake is related to trailing edge effects and the leading edge separation, and how to model this phenomenon and relate it to thrust generation.

The present paper is organized as follows. An introduction of the SD method and different approaches to maintain GCL in both the explicit and implicit time integrations is described in Section 2. Numerical verification studies are shown in Section 3, including a grid refinement study, space discretization accuracy study, time integration accuracy study, and initial condition study. The numerical results for oscillating airfoils are presented in Section 4, along with a simple flow model based on the results. At last, conclusions for the present study are summarized in Section 5.

II. Numerical Approach

Spectral Difference (SD) Method for Dynamic Grids

A high-order Navier-Stokes (N-S) spectral difference solver developed for stationary grids[21,22] has been extended in the present study to moving grids. In the extension, a critical requirement is that the Geometric Conservation Law (GCL)[26] should be satisfied.

In the SD method, all computations are carried out in the computational domain – the standard element. The governing equations are therefore transformed from the physical to the computational domain.

The N-S equation in conservation form reads

$$\frac{\partial Q}{\partial t}+\frac{\partial F}{\partial x}+\frac{\partial G}{\partial y}+\frac{\partial H}{\partial z}=0, \tag{1}$$

where Q is the vector of conservative variables, and F, G, H are the total fluxes including both the inviscid and viscous flux vectors.

After introducing a time-dependent coordinate transformation from the physical domain (t,x,y,z) to the computational domain (τ,ξ,η,ζ) , Equation (1) can be rewritten as

$$\frac{\partial \widetilde{Q}}{\partial t}+\frac{\partial \widetilde{F}}{\partial \xi}+\frac{\partial \widetilde{G}}{\partial \eta}+\frac{\partial \widetilde{H}}{\partial \zeta}=0, \tag{2}$$

where

$$\begin{cases}\widetilde{Q}=|J|Q\\ \widetilde{F}=|J|(Q\xi_t+F\xi_x+G\xi_y+H\xi_z)\\ \widetilde{G}=|J|(Q\eta_t+F\eta_x+G\eta_y+H\eta_z)\\ \widetilde{H}=|J|(Q\zeta_t+F\zeta_x+G\zeta_y+H\zeta_z)\end{cases}$$

Herein, $\tau=t$, and $(\xi,\eta,\zeta)\in[0,1]^3$, are the local coordinates. In the transformation shown above, the Jacobian matrix J takes the following form

$$J=\frac{\partial(x,y,z,t)}{\partial(\xi,\eta,\zeta,\tau)}=\begin{bmatrix}x_\xi & x_\eta & x_\zeta & x_\tau\\ y_\xi & y_\eta & y_\zeta & y_\tau\\ z_\xi & z_\eta & z_\zeta & z_\tau\\ 0 & 0 & 0 & 1\end{bmatrix}.$$

The GCL for the metrics of the transformation can be expressed as

$$\frac{\partial|J|}{\partial t}+\frac{\partial}{\partial\xi}(|J|\xi_t)+\frac{\partial}{\partial\eta}(|J|\eta_t)+\frac{\partial}{\partial\zeta}(|J|\zeta_t)=0. \tag{3}$$

If the mesh undergoes rigid-body motion without deformation, $|J|$ is independent of time. Due to the discretization error, the GCL may not be strictly satisfied if one does not pay attention to how the mesh velocity is computed. In the present study, the GCL error is canceled by adding a source term. Herein, different treatments of the GCL are introduced for both explicit and implicit schemes in light of their respective characteristics. In the explicit method, the following equation

$$\begin{aligned}\frac{\partial|J|Q}{\partial t}&=|J|\frac{\partial Q}{\partial t}+Q\frac{\partial|J|}{\partial t}\\ &=|J|\frac{\partial Q}{\partial t}-Q\left[\frac{\partial}{\partial\xi}(|J|\xi_t)+\frac{\partial}{\partial\eta}(|J|\eta_t)+\frac{\partial}{\partial\zeta}(|J|\zeta_t)\right]\end{aligned} \tag{4}$$

is obvious. Thus Equation (2) can be changed into

$$\begin{aligned}\frac{\partial Q}{\partial t}&=\frac{1}{|J|}\left\{-\left(\frac{\partial\widetilde{F}}{\partial\xi}+\frac{\partial\widetilde{G}}{\partial\eta}+\frac{\partial\widetilde{H}}{\partial\zeta}\right)+Q\left[\frac{\partial}{\partial\xi}(|J|\xi_t)+\frac{\partial}{\partial\eta}(|J|\eta_t)+\frac{\partial}{\partial\zeta}(|J|\zeta_t)\right]\right\}\\ &=\frac{1}{|J|}\left\{-\left(\frac{\partial\widetilde{F}}{\partial\xi}+\frac{\partial\widetilde{G}}{\partial\eta}+\frac{\partial\widetilde{H}}{\partial\zeta}\right)+source\right\}\end{aligned} \tag{5}$$

where

$$source = Q\left[\frac{\partial}{\partial\xi}(|J|\xi_t)+\frac{\partial}{\partial\eta}(|J|\eta_t)+\frac{\partial}{\partial\zeta}(|J|\zeta_t)\right]\cdot$$

The benefits of this method are that the source term is easy to be inserted into the original solver for stationary grids and it can avoid the calculation of $\partial|J|/\partial t$, which might introduce additional errors and increase computational cost.

In the implicit method, according to Sun et al.[22], the computational algorithm is

$$\left(\frac{I}{\Delta t}-\frac{\partial R_c}{\partial \widetilde{Q}_c}\right)\Delta\widetilde{Q}_c = R_c(\widetilde{Q}_c^{\,*})-\frac{\Delta\widetilde{Q}_c^{\,*}}{\Delta t}, \tag{6}$$

where $\Delta\widetilde{Q}_c = \widetilde{Q}_c^{\,n+1}-\widetilde{Q}_c^{\,n}$, c stands for the present cell, and $*$ indicates the most recently updated solutions.

The GCL is introduced in the right-hand side of the equation as

$$\left(\frac{I}{\Delta t}-\frac{\partial R_c}{\partial \widetilde{Q}_c}\right)\Delta\widetilde{Q}_c = R_c(\widetilde{Q}_c^{\,*})-\frac{\Delta\widetilde{Q}_c^{\,*}}{\Delta t}+Q_c^{\,*}\left(\frac{\Delta|J|^*}{\Delta t}+\frac{\partial}{\partial\xi}(|J|^*\xi_t^*)+\frac{\partial}{\partial\eta}(|J|^*\eta_t^*)+\frac{\partial}{\partial\zeta}(|J|^*\zeta_t^*)\right)\cdot \tag{7}$$

It should be noted that in the above equation the discrete form of $\Delta|J|^*/\Delta t$ is exactly the same as $\Delta\widetilde{Q}_c^{\,*}/\Delta t$, which is used to cancel the errors induced by numerical schemes.

III. Simulation Details and Verification Studies

A. Airfoil Motion Control and Mesh Movement Algorithm

In the present study, the airfoil performs a pitching motion expressed as

$$\alpha(t)=\alpha_m+\alpha_0\sin(\omega t+\phi),\ \omega=2\pi f$$

where α_m is the mean angle of attack, α_0 is the amplitude of the pitching angle. The schematic of the airfoil's pitching motion is shown in Figure 1.

Since the mesh undergoes a rigid body motion, the computational grid moves with the body and is updated using

$$\begin{cases} x_{present}-x_c=(x_{former}-x_c)\cos(\Delta\alpha)-(y_{former}-y_c)\sin(\Delta\alpha) \\ y_{present}-y_c=(x_{former}-x_c)\sin(\Delta\alpha)+(y_{former}-y_c)\cos(\Delta\alpha) \end{cases},$$

where (x_c, y_c) is the pitching center, and $\Delta\alpha=\alpha_0(\cos(\omega(t+dt)+\phi_0)-\cos(\omega t+\phi_0))$.

B. Verification Studies

1. Space discretization accuracy and grid refinement studies

In the present study, an initial verification of the orders of accuracy on a coarse mesh ($169\times23\times1$ cells, Figure 2.a) has been conducted at Mach number M_∞=0.5 and Reynolds number Re=5000 for the stationary NACA 0012 airfoil. The skin friction coefficients (Figure 3) using the 3rd- and 4th-order schemes agree well with the results reported by Sun et al.[22] with the separation point calculated at 81.4% chord length for both cases.

A grid refinement study was then performed with dynamic grids and the 3rd-order scheme until the aerodynamic load and wake structures became grid independent, for the k=11.5, St=0.19 case. A group of different grids, with $169\times23\times1$, $169\times47\times1$, $341\times23\times1$, $341\times47\times1$, $685\times23\times1$, $685\times47\times1$, were utilized in the refinement study. From results shown in Figure 4.a and Table 1.a, it can be found that $341\times47\times1$ grid is fine enough to perform the numerical simulation.

Furthermore, the scheme accuracy study for the dynamic grid was performed with the $341\times47\times1$ grid. From the results shown in Figure 4.b, Figure 5 and Table 2.b, it can be concluded that, with the $341\times47\times1$ mesh, the 3rd-order scheme almost works as well as the fourth-order, yet the second-order scheme is too dissipative to be acceptable. Therefore, the $341\times47\times1$ mesh with a 3rd-order SD scheme was used in all the numerical simulations. A similar time refinement study was also carried out, and the numerical results are made sure to be independent of the time step size.

2. Time integration accuracy study for dynamic grids

In order to maintain the accuracy of time integration to be approximately of the 2nd-order for the implicit method, which is also vital for the vortex-dominated flow, a time refinement study is conducted in the present study. In this section, an isentropic vortex propagation problem is used to verify the time integration accuracy of a dynamic grid.

Referring to F. Q. Hu et al.[24], the velocity field of the isentropic vortex is written as

$U(r) = \frac{U'_{\max}}{b} r e^{\frac{1}{2}(1-\frac{r^2}{b^2})}$, where b is the radius of the position where $U'_{\max}$ occurs.

Therefore, the horizontal and vertical components could be written as

$$\begin{cases} u = -U(r)\sin\theta \\ v = U(r)\cos\theta \end{cases}, \text{ where } r = \sqrt{(x-x_c)^2 + (y-y_c)^2}.$$

Other initial distributions can be written as

$$\rho(r) = (1-\frac{1}{2}(\gamma-1)U'^2_{\max} e^{1-\frac{r^2}{b^2}})^{1/(\gamma-1)}, \quad p(r) = (1-\frac{1}{2}(\gamma-1)U'^2_{\max} e^{1-\frac{r^2}{b^2}})^{\gamma/(\gamma-1)}.$$

The free stream velocities are set to be $u_0 = 0.5$,and $v_0 = 0$, and other initial conditions are given as $U'_{\max} = 0.5u_0 = 0.25$, $b = 0.2$. According to the work of Mavriplis and Nastase[25], in order to eliminate the errors introduced by the space discretization scheme, the result obtained with the time step of 0.001 is treated as the 'exact' solution. The results of the time refinement study are given in Table 2 (only the 2nd-order verification is shown) and Figure 6. Obviously, the present numerical method maintains the time integration accuracy.

3. Studies of effects of initial conditions

Several methods have been tried to set up initial conditions, and herein, two of them, namely the harmonic initial velocity distribution method and the steady solution method, are compared and discussed. The so-called "harmonic initial velocity distribution method" uses a smoothly changed velocity field as the initial velocity distribution. The algorithm is shown as below,

$$r < r_0, \quad u = v = w = 0,$$

$$r_0 \le r < 2r_0, \begin{cases} u = u_0(\sin(\pi(\frac{r-r_0}{r_0} - \frac{1}{2})) + 1)/2 \\ v = v_0(\sin(\pi(\frac{r-r_0}{r_0} - \frac{1}{2})) + 1)/2 \\ w = w_0(\sin(\pi(\frac{r-r_0}{r_0} - \frac{1}{2})) + 1)/2 \end{cases},$$

$$r \ge 2r_0, \quad u = u_0, v = v_0, w = w_0,$$

The so-called "steady solution method" uses the steady solution as the initial condition. According to B.1 of the present section, it has been shown that the steady solution exists and is accurate enough with 3rd-order scheme. Furthermore, considering the general experimental procedures (do not collect data till the wind/water tunnel runs to a stable condition) and that all the cases in the present study started from AoA=0°, this method might be a good choice. Some results are shown in Figure 7. Together with the comparison between numerical and experimental results, which will be shown in the next section, the steady solution method is suitable for the present study, while the harmonic initial velocity distribution method does not seem to agree well with the real physics.

IV. Numerical Results and Discussions

An overview of the cases simulated in the present study is listed in Table 3. In the following parts, analyses of these vortex-dominated flow fields will be shown.

A. Comparison with experimental and other numerical results

Unsteady numerical simulations were conducted for the NACA 0012 airfoil undergoing a sinusoidal pitching motion at Mach number M_∞=0.1, and Reynolds number Re=12600. Flows at three different reduced frequencies, k=5.2, 5.7, 11.5, but the same angle amplitude α_0= 2° were firstly computed and analyzed. Table 4 shows the comparison of the mean thrust coefficient obtained with different methods. It is found that the Mach number

significantly affects the mean thrust coefficient in the present numerical simulation, similar to Young's results[2]. In his research, when the inlet Mach number is set to be 0.2, the mean thrust coefficient is -0.040 for the case Re=12000, k=11.5, St=0.19. In the present study, this coefficient is -0.041 for the case Re=12600, k=11.5, St=0.19, while if the inlet Mach number is 0.1, the mean thrust coefficient is 0.031, close to the experimental one. Though in the experiment, Mach number is extremely small (in the water tunnel), in the present numerical simulation, it seems that Mach number M_∞=0.1 is suitable for the studied problems.

According to Bohl and Koochesfahani[1], a neutral wake is obtained at $\alpha_0 = 2^\circ$ and k=5.70 in a water tunnel experiment. From the numerical results (Figure 8,9,10), it seems that the neutral wake is generated at a certain reduced frequency between 5.20 and 5.70. From Figure 8 and Figure 9, the averaging flow field can show the general flow features of different reduced frequencies and help to better distinguish the thrust-generation wakes from the drag-generation wakes. Taking into account the inlet Mach number effect in the simulation as mentioned before, the agreement between the experiment and numerical results is quite good.

Figure 11 shows the thrust coefficient time histories of the three reduced frequencies: 11.5, 5.7, 5.2. It should be noted that the thrust coefficients in these cases are very small (also seen in the averaged values in Table 4). This might be due to the relatively small Strouhal number (St<0.5), which means that the flow is in the "quasi-steady" regime as suggested by Hu et al.[8]. In the section of extended numerical results, the effect of Strouhal number will be further discussed.

B. Extended numerical results

For all cases studied below, the airfoil motions are sinusoidal with the inlet Mach number M_∞=0.1, and Reynolds number Re=12600.

1. Effects of Strouhal number

In this section, cases with the same reduced frequencies but different Strouhal numbers will be discussed. From Table 3 and Figure 12.a, it can be found that at k=11.5, both mean and peak thrust will grow steadily as the Strouhal number increases. It is obvious that when leading edge separation appears (under the condition of the high Strouhal number), the shape of the thrust coefficient history will change from a sinusoidal one to a 'quasi-periodic' and then a non-periodic one. This indicates that vortices generated by leading edge separation could significantly influence the ways of thrust generation, and to some extent (at least in the context of the present study), the interaction between trailing edge effects and leading edge separations is beneficial for the thrust generation. The same trend can be generalized for the case k=5.7 (Figure 12.b).

In order to further study the flow features, flow fields are desirable for analysis. Figure 10 and Figure 15.a,b show several vorticity fields of different Strouhal numbers at k=11.5. It is obvious that at small Strouhal numbers, trailing edge effects dominate the flow field, while as the Strouhal number increases, the leading edge separation becomes more and more severe, and the interaction between the leading edge separation and trailing edge effects become prominent for the formation of the wake structure. Upon Close observation of the leading edge separation in Figure 15, it can be found that the separation seems to be inclined to one side of the airfoil, which is determined by the initial conditions.

Another important phenomenon is concerning the deflected wake structure. Although all the initial conditions are symmetric, asymmetric phenomena can be generated because of nonlinear behaviors of vortex arrays in the wake. From Figure 14, it can be found that the deflection direction of the wake is determined by the initial phase of the pitching motion, with all other variables kept constant. It can be seen from Table 3 and Figure 12 that an asymmetric wake is accompanied with the 'quasi-periodic' or unsteady thrust generation. In terms of the above analyses, it can be concluded that to some extent, asymmetric wakes are beneficial for thrust generation.

2. Effects of reduced frequency

In this section, cases with the same Strouhal numbers but different reduced frequencies will be discussed. It can be found from Table 2 and Figure 13 that, at the same Strouhal number, a higher mean and peak thrust coefficient can be obtained with a smaller reduced frequency (corresponding to larger pitching angle amplitude).

From Figure 13, it can also be found that smaller reduced frequencies make the thrust coefficient history depart more from the sinusoidal shape. From the discussions in B.1 of the present section, it is clear that at reduced frequency k=11.5, this shape modification of the thrust coefficient history is due to the leading edge separation. However, herein, from Table 2 and Figure 13.a, at k=5.7, even leading edge separation does not appear, the shape of the thrust coefficient history still exhibits certain unsteady features. One reasonable explanation is that since the pitching frequency reduces when reduced frequency decreases, there is enough time for the shear flow from the side

boundary layer of the airfoil to interact with the vortices generated through trailing edge moving. Even at higher reduced frequencies, this effect also exists. However, because of the short contact time, this phenomenon is suppressed. Still, it can be confirmed that the interaction between flow structures from side boundary layer and wake vortices can enhance the thrust generation. Further investigation of flow field in Figure 15 shows that the onset of the leading edge separation seems to be only related to the Strouhal number (also seen in Table 3), but the separation mode is determined both by the Strouhal number and the reduced frequency.

3. Overview of all the results

It has been widely accepted that the thrust generated by the flapping motion is due to the reverse Von Karman vortex street, and the present results are of no exception. From Figure 16, it is obvious that in the same region behind the airfoil, the vorticity in (b) is much stronger than that in (a), meaning that high velocity gradient region is larger in (b) than in (a). The more important feature of the figures is that the number of vortices in (b) is less than that in (a). Since the reduced frequency is the same in the two figures, the only possible explanation is that vortices in (b) move faster than those in (a). This means that for the relatively high Strouhal number, the vortex pair formed after one pitching-up-and-pitching-down stroke can accelerate in a certain distance after the airfoil, which further can lead us to the conclusion that such vortex structures can extract more energy from the flow field than the traditional reverse von Karman vortex street.

The general physical process can be described as followed. The trailing edge motion transmits the kinetic energy to the flow via viscous effects (in the inviscid theory, this is treated as Kutta conditions). This process determines the circulation (energy stored in the form of deformation) shed into the flow field, and just after one stroke, the concentration of vorticity is extremely high in the vicinity of the trailing edge. Thus, in the reverse Von Karman vortex street, the large velocity gradient actuates the vortex/vortex pair to accelerate. During this course, the deformation energy of the flow is released in the form of kinetic energy. Quite possibly, the vortex pair can release more deformation energy, which can be proved by the nonlinear increase of the mean thrust coefficient shown in Table 3 for the cases with the same reduced frequencies but different Strouhal numbers. The corresponding effect is to generate a counterforce --- thrust on the airfoil.

Herein, two features of this energy transformation process should be further mentioned. One is that based on the above discussion this process should greatly depend on the vortex sheet formation (therefore, the phenomena are strongly related to aerodynamic parameters, like Strouhal number and reduced frequency), which closely influences the energy storage-and-release process. The other is that since the viscous force plays an important role during the transformation and the nature of this force is dissipated, higher vorticity strength must accompany with more energy waste. This could be verified through Figure 13.b that smaller reduced frequency is more beneficial for the thrust generation under the same Strouhal number.

C. Modeling of flow structures

Based on the former discussion, flow models are set up in the present section to further explain the formation of the deflected wake with the symmetric initial conditions. A semi-infinite vortex array is considered for the modeling in term of generality and simplicity.

First of all, we assume that all the vortices in Figure 18 are isentropic and of the same strength. The velocity field has been given before (in the Section 3, B.2), and herein, all the formulas are non-dimensionalized as below:

$$\frac{U(r)}{U'_{\max}} = \frac{r}{b} e^{\frac{1}{2}(1-\frac{r^2}{b^2})} \Rightarrow \overline{U} = \bar{r} e^{\frac{1}{2}(1-\bar{r}^2)}, \text{ where } \overline{U} = \frac{U(r)}{U'_{\max}}, \bar{r} = \frac{r}{b}.$$

In the following discussion, all distances are non-dimensionalized with b and all velocities are non-dimensionalized with $U'_{\max}$.

1. Equally-spaced vortex array

As shown in Figure 17.a, only the behavior of Vor1 in the induced velocity field formed by all the other vortices is considered. This could help to investigate the onset of the deflected wake and the stability conditions of the whole vortex array. The velocity difference in the vertical direction experienced by Vor1 can be generalized as

$$\overline{V_{diff}} = \overline{V_{up}} - \overline{V_{down}} = \left(\sum_{i=1}^{n} 2ie^{\frac{1}{2}(1-(2i\overline{C})^2)} - \sum_{j=1}^{m} (2j-1)e^{\frac{1}{2}(1-(((2j-1)\overline{C})^2+(2\overline{D})^2))} \right) \overline{C},$$

where i, j indicates the position of the vortex in the upper and lower row, respectively.

From figure 18.a, it can be found that i,j=10 is enough for the semi-infinite vortex array analysis. The main feature of this figure is that if these isentropic vortices are equally spaced, the first vortex can remain stable with a

wide range of parameters C and D. Using the superposition method, it is reasonable to conclude that if the first vortex could remain stable, all the other vortices in the array will remain stable and therefore, the whole system will remain stable.

2. Dipole

Careful observation of the flow fields with the deflected wakes tells that the vortex array seems to consist of infinite dipoles. Godoy-Dinan et al.[13] have used the 'dipole' concept to set up the model for deflected wakes. In their approach, they treated the dipole as the combination of two point vortices. Herein, the dipole is the combination of two isentropic vortices. The velocity difference in the vertical direction experienced by the first dipole can be generalized as

$$\overline{V_{diff}} = \overline{V_{up}} - \overline{V_{down}} = \sum_{i=1}^{n} (i\overline{L_1} - \overline{L_2}) e^{\frac{1}{2}(1-((i\overline{L_1}-\overline{L_2})^2+\overline{D}^2))} - \sum_{j=1}^{n} (j\overline{L_1} + \overline{L_2}) e^{\frac{1}{2}(1-((j\overline{L_1}+\overline{L_2})^2+\overline{D}^2))} - \overline{r_c} e^{\frac{1}{2}(1-\overline{r_c}^2)} \frac{\overline{L_2}}{\sqrt{\overline{L_2}^2 + \overline{D}^2}}$$

where $r_c = 2\sqrt{L_2^{\,2} + D^2}$ and $\overline{r_c} = \frac{r_c}{b}$, i, j indicates the position of the vortex in the upper and lower row, respectively.

In this case, it has been verified that i,j=10 is enough for the analysis. From Figure 18.b it can be found that if the distance between the adjacent vortex pairs is long enough, the first dipole will definitely move downwards (the first vortex is positive) or upwards (the first vortex is negative).

In the real cases, the closeness (suggested by Platzer et al.[10]) between the adjacent two vortices or the vorticity from the side boundary layer and the leading edge separation can contribute to the formation of the dipole. The later can also be treated as a kind of disturbance, which could affect the practical behavior of the vortex array.

V. Conclusion

The compressible N-S flow solver with a high-order SD method has been successfully extended in the present research to simulate the unsteady flow induced by the pitching motion of a NACA 0012 airfoil. With different approaches, GCL has been efficiently introduced for both the explicit and implicit time integrations. It has been shown that the present algorithm for GCL works well with the SD method. The present simulations are compared with experimental results and other numerical simulations. Promising agreement has been obtained. Based on the numerical simulation, several conclusions can be drawn:

1. Flow with larger Strouhal numbers can generate more thrust on the oscillating airfoil than that with smaller Strouhal numbers. For the same Strouhal number, small reduced frequency (large pitching angle amplitude) is more beneficial for thrust generation. Wake vortex array with a small Strouhal number is mainly dominated by trailing edge effects, while the wake structure under large Strouhal numbers is complex because of the interaction of leading edge separation and trailing edge effects.

2. For the small Strouhal number, the wake structure will remain symmetric if the initial mean AOA is zero, meaning that the vortex array could remain stable by itself. While for the large Strouhal number, due to the vortex instability and relatively larger disturbances, asymmetric wake structures will appear. A simple flow model is developed to explain the formation of different wake structures.

References

[1]D. G. Bohl, M. M. Koochesfahani, MTV measurements of the vertical field in the wake of an airfoil oscillating at high reduced frequency, J. Fluid Mech. (2009), vol. 620, pp. 63-88.

[2]J. Young, J. C. S. Lai, Oscillating frequency and amplitude effects on the wake of a plunging airfoil, AIAA J. (2004), vol. 42, No.10, pp. 2042-2052.

[3]J. Young, Numerical simulation of the unsteady aerodynamics of flapping airfoils, PhD. Thesis (2005).

[4]K. D. von Ellenrieder, K. Parker, J. Soria, Fluid mechanics of flapping wings, Experimental Thermal and Fluid Science (2008), vol. 32, pp. 1578-1589.

[5]R. Godoy-Diana, J. Aider, J. E. Wesfreid, Transition in the wake of a flapping foil, Physical Review E (2008), vol. 77.

[6]C. Kang, Y. Baik, L. Bernal, M.V. Ol, W. Shyy, Fluid Dynamics of Pitching and Plunging Airfoils of Reynolds Number between 1.0×10^4 and 6.0×10^4 (2009), AIAA Paper, No. 2009-536.

[7]C. Kang, H. Aono, P. Trizila, Y. Baik, J. Rausch and L. Bernal, Modeling of Pitching and Plunging Airfoils at Reynolds Number between 1×10^4 and 6×10^4 (2009), AIAA Paper, No. 2009-4100.

[8]H. Hu, A. G. Kumar, G. Abate, R. Albertani, An experimental study of flexible membrane wings in flapping flight (2009), AIAA Paper, No. 2009-0876.

[9]K. D. Jones, C. M. Dohring, and M. F. Platzer, Experimental and computational investigation of the Knoller-Betz effect, AIAA J. (1998), vol. 36, No.7, pp. 1240-1246.

[10]M. F. Platzer, K. D. Jones, J. Young, J. C. S. Lai, Flapping-wing aerodynamics: progress and challenges, AIAA J. (2008), vol. 46, No.9, pp. 2136-2149.

[11]G. C. Lewin, H. Haj-Hariri, Modeling thrust generation of a two-dimensional heaving airfoil in a viscous flow, J. Fluid Mech. (2003), vol. 492, pp. 339-362..

[12]K. D. von Ellenrieder, S. Pothos, PIV measurement of the asymmetric wake of a two dimensional heaving hydrofoil, Exp. Fluids (2007), vol. 43, No. 5.

[13]R. Godoy-Diana, C. Marais, J. Aider, J. E. Wesfreid, A model for the symmetric breaking of the reverse Benard-von Karman vortex street produced by a flapping foil, J. Fluid Mech. (2009), vol. 622, pp. 23-32.

[14]L. Tang, J. D. Baeder, Improving Godunov-type reconstructions for simulation of vortex-dominated flows, J. Comput. Phys. (2006), vol. 213, pp. 659-675.

[15]C. L. Liang, S. Premasuthan, A. Jameson, Z. J. Wang, Large eddy simulation of compressible turbulent channel flow with spectral difference method (2009), AIAA Paper, No. 2009-402

[16]M. R. Visbal, D. V. Gaitonde, On the use of high-order finite-difference schemes on curvilinear and deforming meshes, J. comput. Phys. (2002), vol. 181, pp. 155-185.

[17]Z. J. Wang, High-order methods for the Euler and Navier Stokes equations on unstructured grids, Progress in Aerospace Science (2007), vol. 43, pp. 1-41.

[18]Y. Liu, M. Vinokur, Z. J. Wang. Discontinuous spectral difference method for conservation laws on unstructured grids, J. Comput. Phys. (2006), vol. 216, pp. 780–801.

[19]Z. J. Wang, Y. Liu, G. May, A. Jameson, Spectral difference method for unstructured grids II: extension to the Euler equations, J. Sci. Comput. (2007), vol. 32, pp. 45–71.

[20]G. May, A. Jameson, A spectral difference method for the Euler and Navier–Stokes equations(2006), AIAA Paper, No.2006–304.

[21]Y. Z. Sun, Z. J. Wang, Y. Liu, High-order multidomain spectral difference method for the Navier-Stokes equations on unstructured hexahedral grids, Commun. Comput. Phys. (2006), vol. 2, No. 2, pp. 310-333.

[22]Y. Z. Sun, Z. J. Wang, Y. Liu, Efficient implicit non-linear LU-SGS approach for compressible flow computation using high-order spectral difference method, Commun. Comput. Phys. (2009), vol. 5, No. 2-4, pp. 760-778.

[23]P. O. Persson, J. Peraire, J. Bonet, Discontinuous Galerkin solution of the Navier-Stokes equations on deformable domains, Computer Methods in Applied Mechanics and Engineering (2009), vol. 198, pp. 1585-1595.

[24]F. Q. Hu, X. D. Li, D. K. Lin, Absorbing boundary conditions for nonlinear Euler and Navier-Stokes equations based on the perfectly matched layer technique, J. Comput. Phys. (2008), vol. 227, pp. 4398-4424.

[25]D. J. Mavriplis, C. R. Nastase, On the geometric conservation law for high-order discontinuous Galerkin Discretizations on dynamically deforming meshes, AIAA paper, 2008-778.

[26]P. D. Thomas, C. K. Lombard, Geometric conservation law and its application to flow computations on moving grids, (1979), AIAA J. vol. 17, pp. 1030-1037.

[27]M. R. Visbal, High-fidelity simulation of transitional flows past a plunging airfoil(2009), AIAA Paper, No. 2009-391.

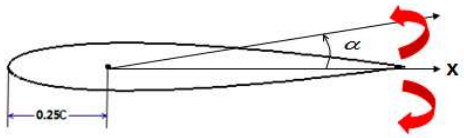

FIGURE 1. The schematic of airfoil's pitching motion. In the present study, $\alpha_m = 0^\circ$ (zero mean angle of attack (AOA)), and the pitching angle amplitude defined in the paper is α_0, corresponding to a the peak to peak amplitude of $2\alpha_0$.

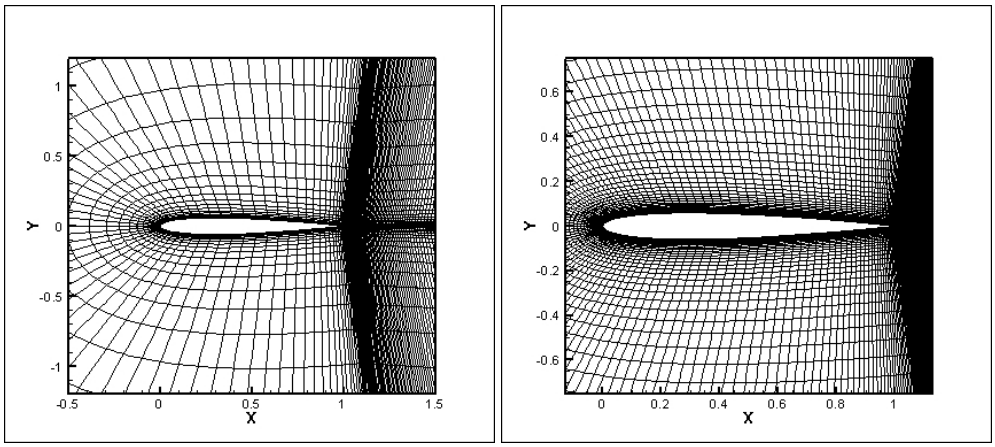

FIGURE 2. Several meshes for the verification study (a. $169\times23\times1$, b. $341\times47\times1$, c. $685\times47\times1$).

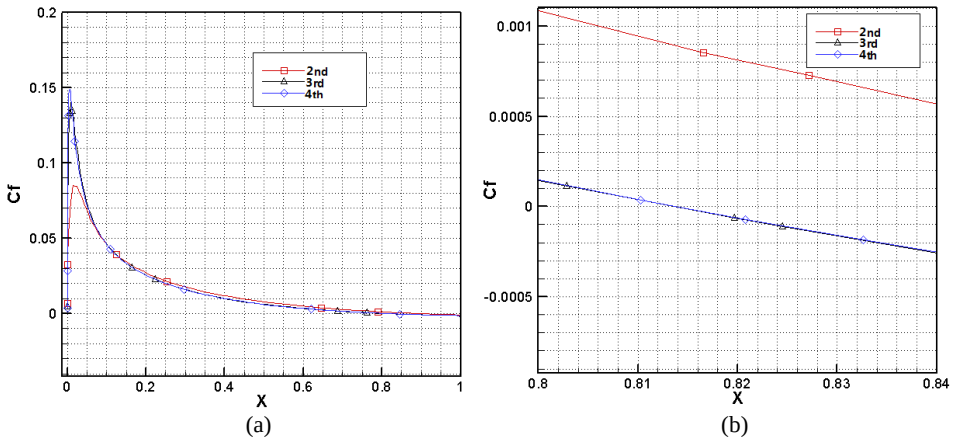

FIGURE 3. Comparison of the skin friction coefficients using schemes of different orders of accuracy. $Ma = 0.5, \mathrm{Re} = 5000$

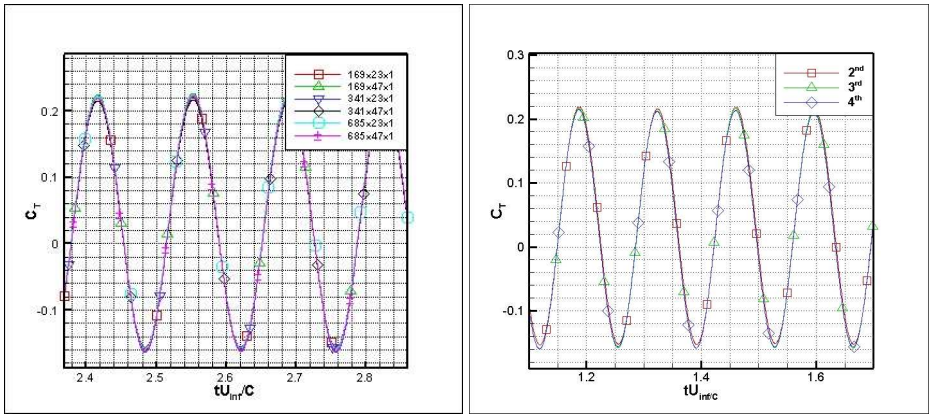

(a) (b)

FIGURE 4. a. Comparison of the thrust coefficients using different meshes with 3rd-order scheme. b. Comparison of the thrust coefficients using the medium mesh ($341\times47\times1$) with schemes of different orders of accuracy. $St=0.19, k=11.5$.

a.

	169×23	341×23	685×23	169×47	341×47	685×47	341×95
$\overline{C_T}$	0.032	0.034	0.034	0.029	0.031	0.031	0.031

Note: Implicit schemes with the time integration of 2nd-order and the spatial discretization of 3rd-order for all the cases.

b.

	2nd	3rd	4th
$\overline{C_T}$	0.034	0.031	0.030

Note: Implicit schemes with the time integration of 2nd-order for all the cases. Cells number of the mesh is $341\times47\times1$.

TABLE 1. Mean thrust coefficients for grid refinement and scheme accuracy study

$\omega_z * C / U_\infty$

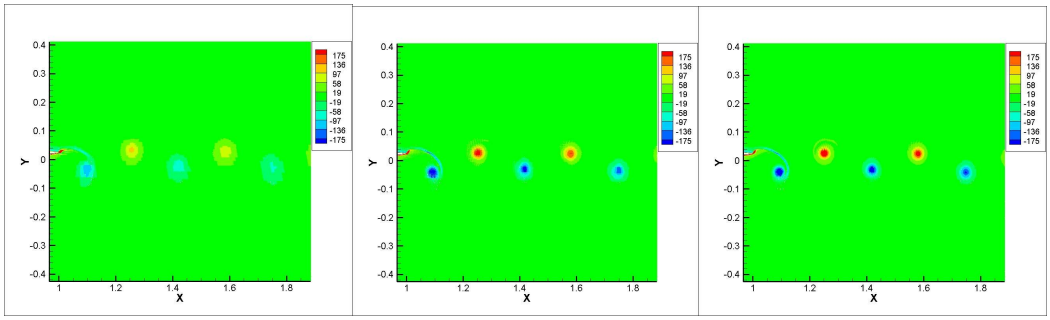

FIGURE 5. Comparison of the vorticity fields using the medium mesh ($341\times47\times1$) with schemes of different orders (from left to right: 2nd, 3rd, 4th). $St=0.19, k=11.5$.

T-2nd

Δt	Euler		N-S	
	L1error	Accuracy	L1error	Accuracy
0.1	1.626E-004		1.601E-004	
0.04	3.486E-005	1.680	3.414E-005	1.686
0.02	9.750E-006	1.838	9.513E-006	1.843
0.01	2.592E-006	1.911	2.511E-006	1.922
0.005	6.374E-007	2.024	6.135E-007	2.033
0.002	7.646E-008	2.314	7.315E-008	2.321

'exact': $\Delta t = 0.001$

Table 2. L1 norm and time integration accuracy

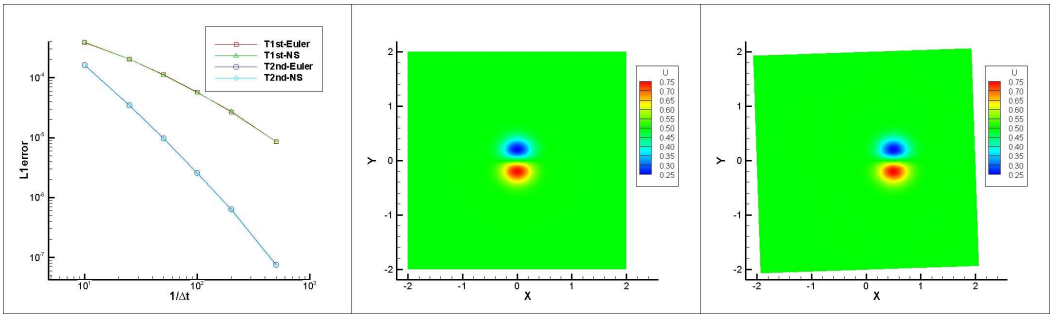

(a) (b) (c)

FIGURE 6. a. Time integration accuracy b. Initial velocity distribution for the isentropic vortex c. Velocity distribution after t=1.0s, with Euler equations.

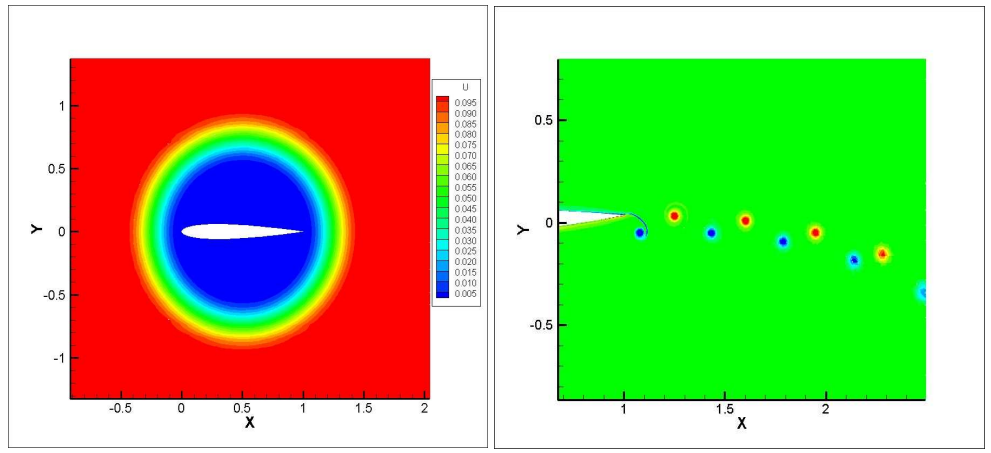

(a) (b)

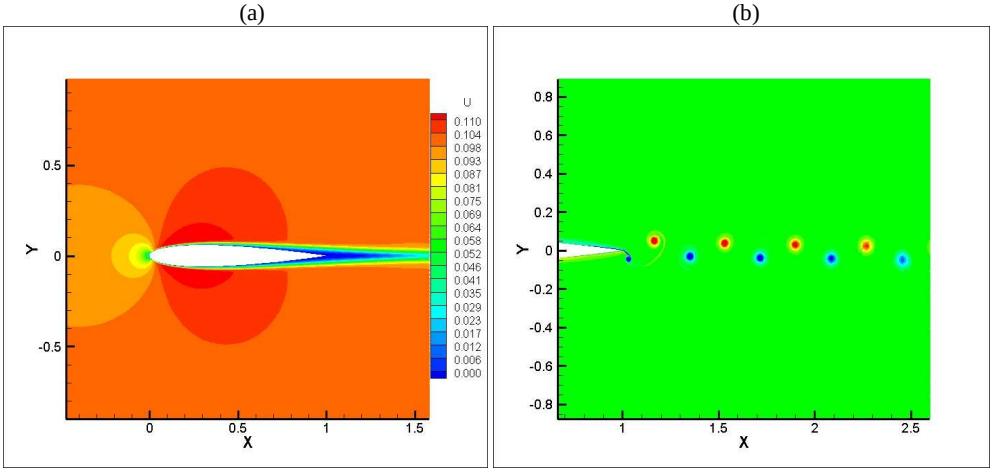

(c) (d)

FIGURE 7. a. Harmonic initial velocity distribution b. Simulated vorticity field after approximately 24 cycles using a harmonic initial velocity distribution c. Velocity (Mach number) contour of the steady solution d. Simulated vorticity field after approximately 24 cycles using the steady solution as initial conditions

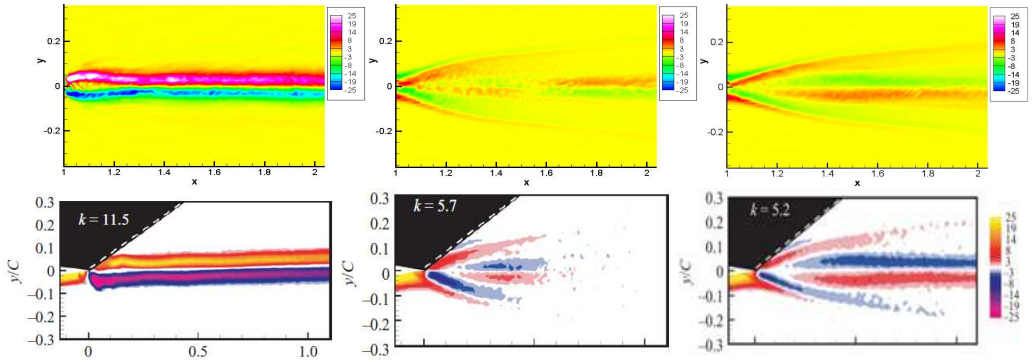

FIGURE 8. Averaged vorticity field in the wake of the oscillating airfoil for three reduced frequencies (from left to right: 11.5, 5.7, 5.2), $\alpha_0 = 2^\circ$. (All contour scales are the same as those of the experimental results; all experimental results are from the literature[1])

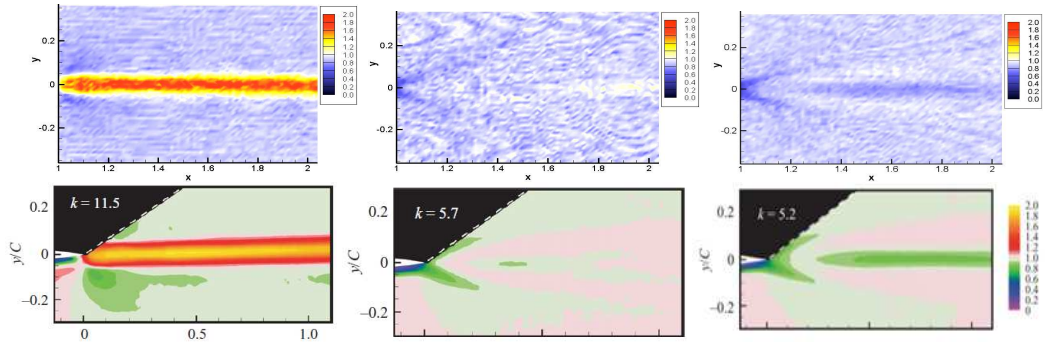

FIGURE 9. Averaged velocity field in the wake of the oscillating airfoil for three reduced frequencies (from left to right: 11.5, 5.7, 5.2), $\alpha_0 = 2^\circ$. (All contour scales are the same as those of the experimental results; all experimental results are from the literature[1])

St	k	A/C	$\overline{C_T}$	Reversed BvK wake	Deflected wake	LE Separation
0.19	11.5	0.0524	0.031	Y.	N.	N.
0.20	11.5	0.0546	0.036	Y.	N.	N.
0.25	11.5	0.0683	0.076	Y.	N.	N.
0.33	11.5	0.0911	0.16	Y.	Y.	N.
0.50	11.5	0.1366	0.50	Y.	Y.	Y.
0.63	11.5	0.1707	0.74	Y.	Y.	Y.
0.10	5.7	0.0524	-0.015	Y.	N.	N.
0.25	5.7	0.1378	0.12	Y.	N.	N.
0.33	5.7	0.1837	0.23	Y.	Y.	N.
0.50	5.7	0.2750	0.56	Y.	Y.	Y.
0.63	5.7	0.3445	0.83	Y.	Y.	Y.
0.33	24	0.0436	0.035	Y.	Y.	N.
0.33	34.5	0.0304	0.017	Y.	Y.	N.
0.50	34.5	0.0455	0.072	Y.	Y.	Y. (little)
0.09	5.2	0.0524	-0.018	N.	N.	N.

Note: '-' for the mean thrust coefficient means drag.

TABLE 3. An overview of the simulation information

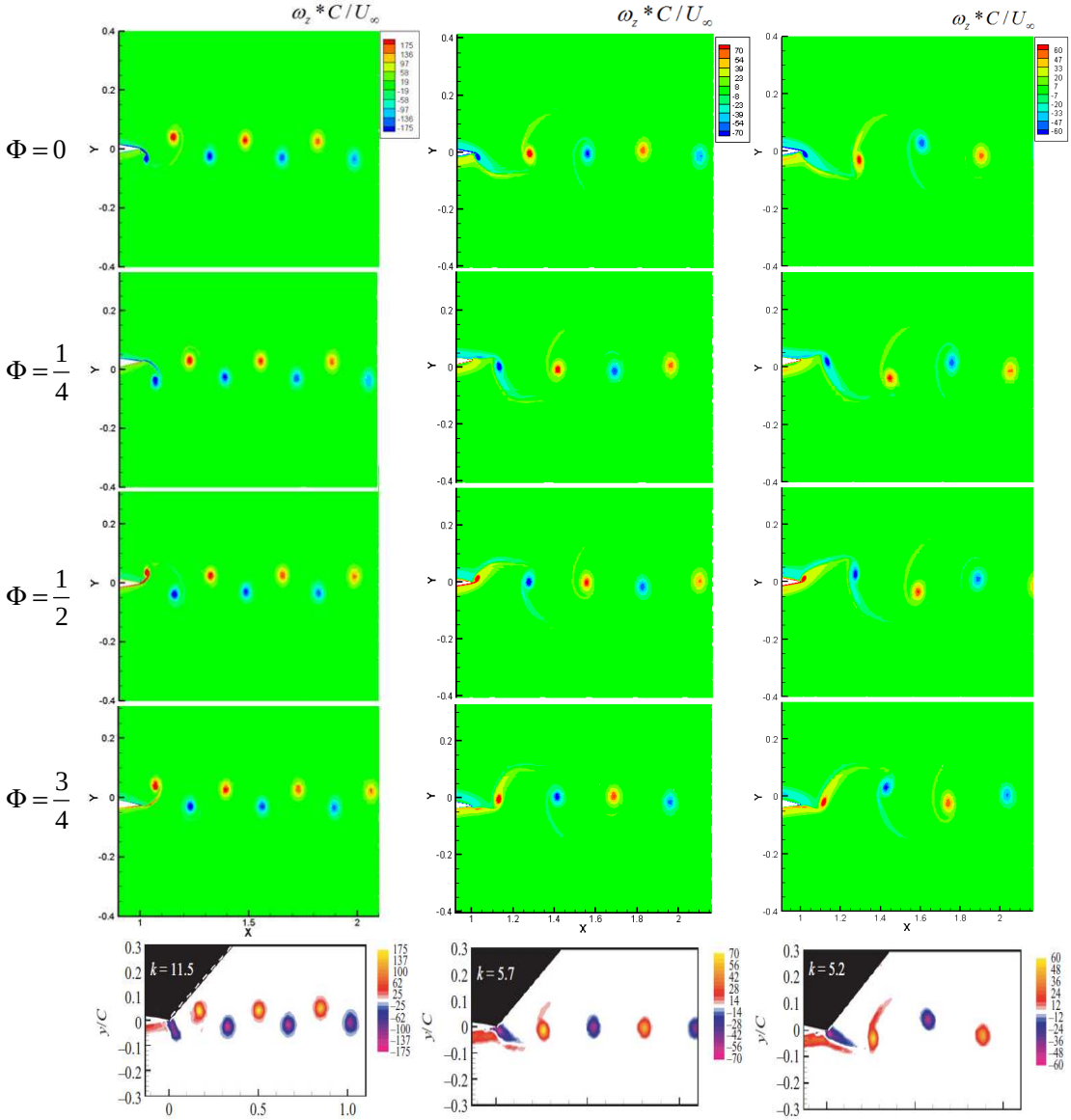

FIGURE 10. Top: Instantaneous vorticity field in the wake of the oscillating airfoil for three reduced frequencies (from left to right: 11.5, 5.7, 5.2), $\alpha_0 = 2^\circ$; Down: Phase-averaged vorticity field from the experiment, $\alpha_0 = 2^\circ$. (All experimental results are from the literature[1].)

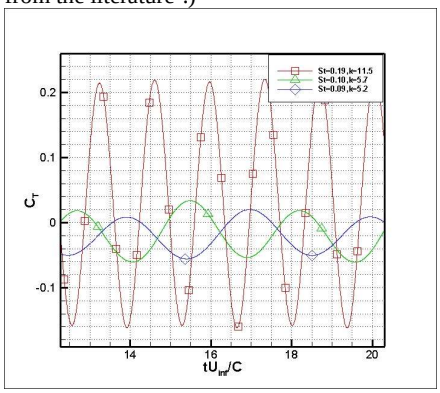

FIGURE 11. Thrust coefficient histories for $k = 11.5, 5.7, 5.2, \alpha_0 = 2^\circ$

Re=12600, Ma=0.1

St	k	A/C	$\overline{C_T}$	Exp. $\overline{C_T}$
0.19	11.5	0.0524	0.031	0.024
0.10	5.7	0.0524	-0.015	-0.026
0.09	5.2	0.0524	-0.018	-0.030

TABLE 4. Mean thrust coefficients comparison

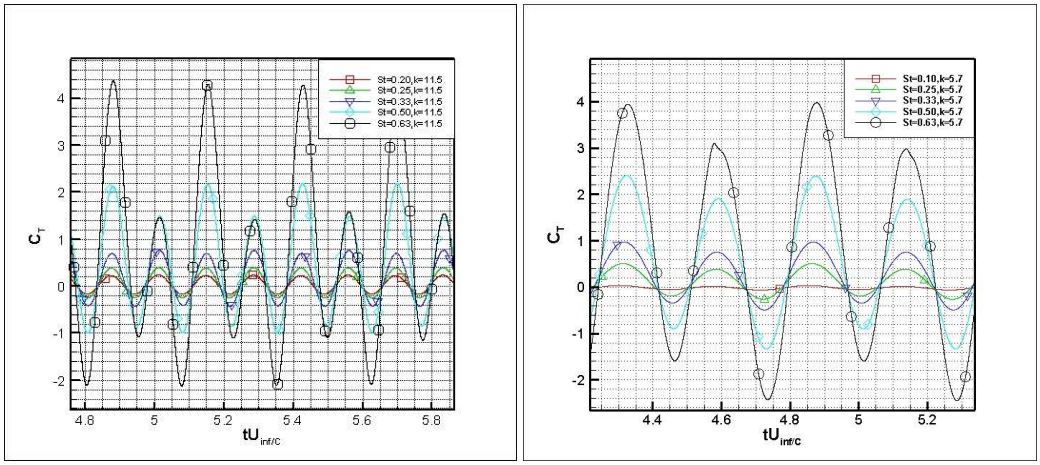

(a) (b)

FIGURE 12. Thrust coefficient histories of the same reduced frequeny. a. $k = 11.5$, b. $k = 5.7$.

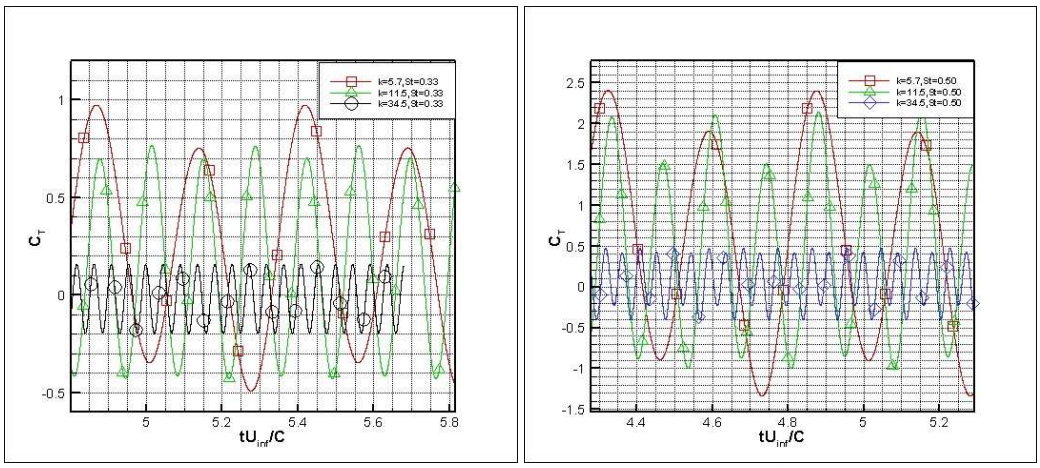

(a) (b)

FIGURE 13. Thrust coefficient histories of the same Strouhal number. a. $St = 0.33$, b. $St = 0.5$.

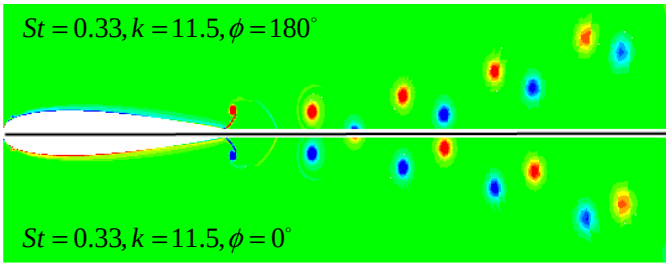

FIGURE 14. Comparison of the vorticity fields for different initial phases, after 24 cycles.

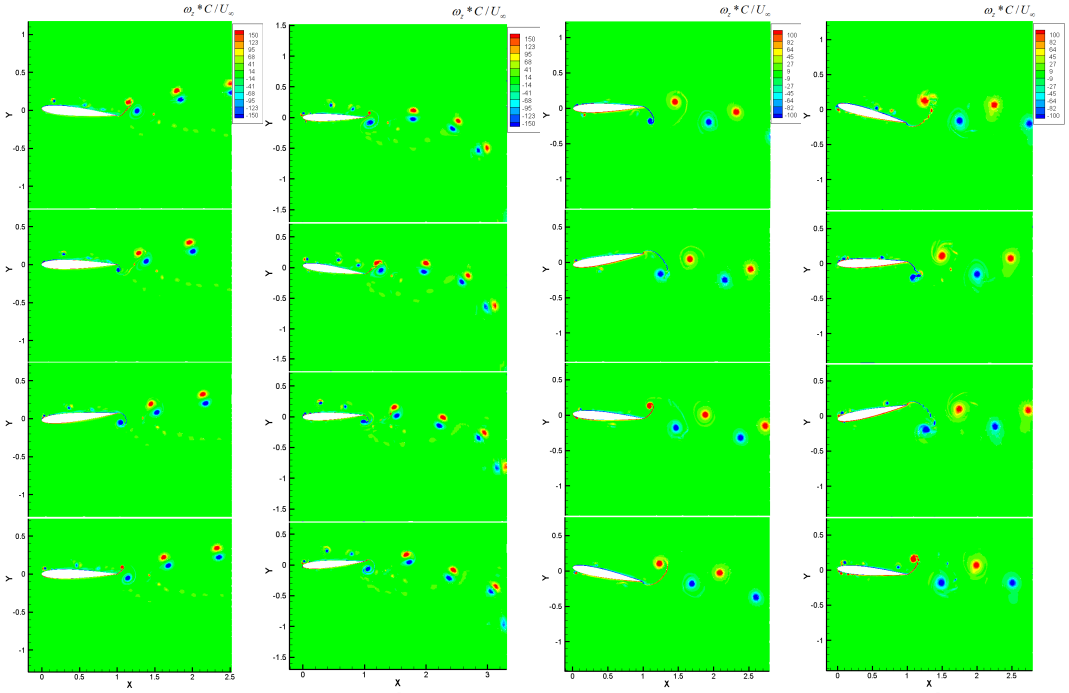

(a) (b) (c) (d)

FIGURE 15. Instantaneous vorticity fields with leading edge separation. a. $St = 0.50, k = 11.5$, b. $St = 0.63, k = 11.5$, c. $St = 0.50, k = 5.7$, d. $St = 0.63, k = 5.7$.

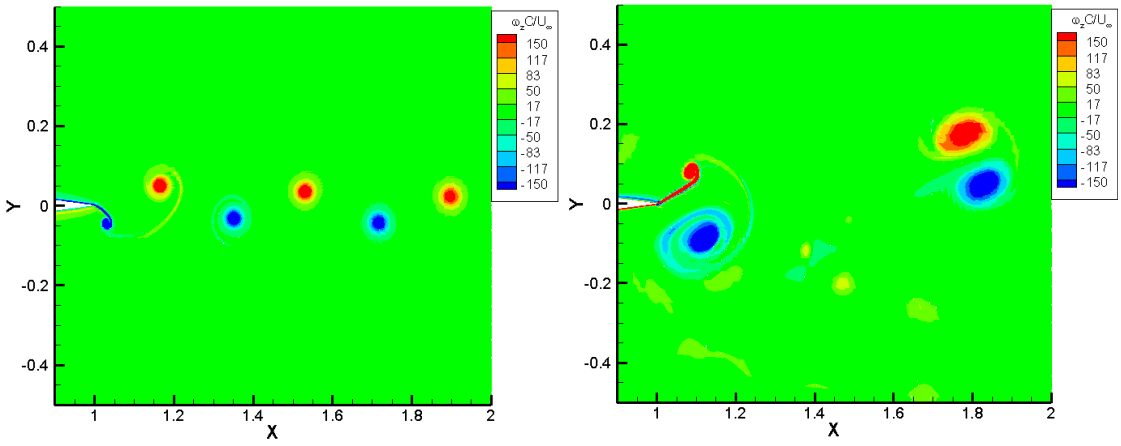

(a) (b)

FIGURE 16. Vorticity fields in the same region behind the airfoil. a. $St = 0.25, k = 11.5$,b. $St = 0.63, k = 11.5$.

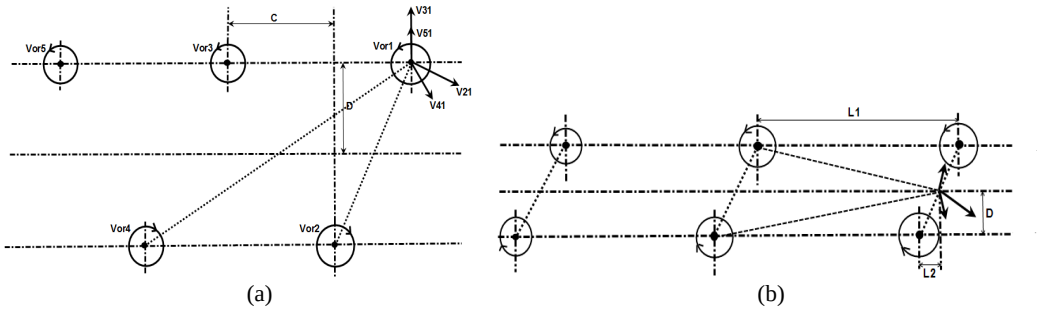

(a) (b)

FIGURE 17. Schematic of the vortex array models.

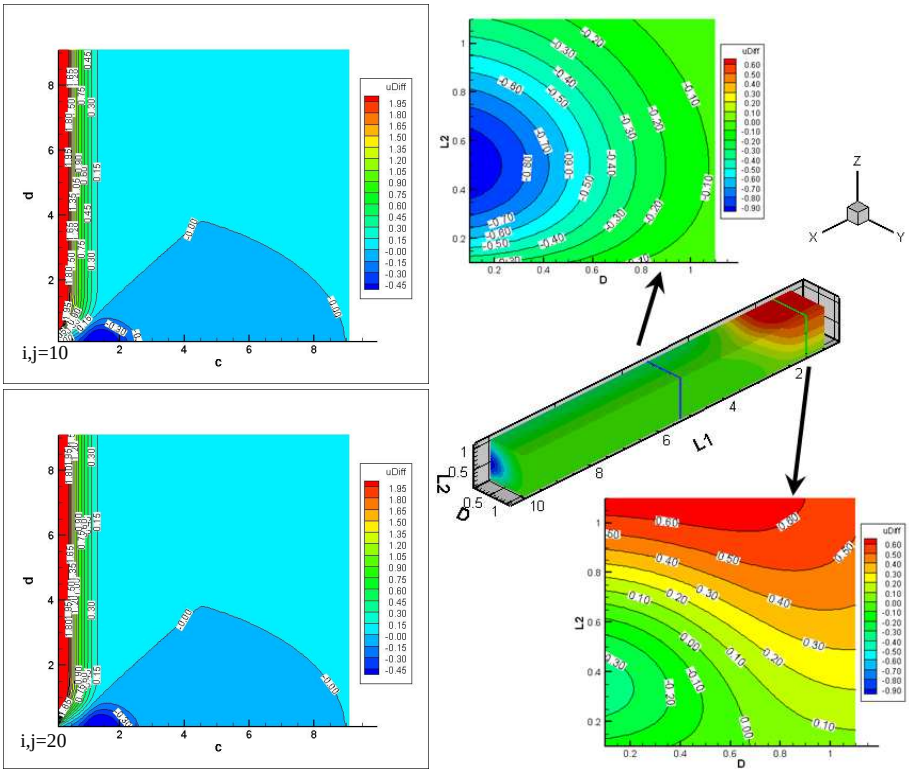

(a) (b)

FIGURE 18. Velocity differences in the vertical direction for different flow models.